A grating-based single-shot x-ray phase contrast and diffraction method for *in vivo* imaging

Eric E. Bennett,[a] Rael Kopace, Ashley F. Stein, and Han Wen[b]
National Heart, Lung, and Blood Institute, National Institutes of Health, Imaging Physics Section, Translational Medicine Branch, 10 Center Drive, MSC 1061, Bethesda, Maryland 20892

(Received 27 May 2010; revised 30 August 2010; accepted for publication 7 September 2010; published 29 October 2010)

Purpose: The purpose of this study is to develop a single-shot version of the grating-based phase contrast x-ray imaging method and demonstrate its capability of *in vivo* animal imaging. Here, the authors describe the principle and experimental results. They show the source of artifacts in the phase contrast signal and optimal designs that minimize them. They also discuss its current limitations and ways to overcome them.
Methods: A single lead grid was inserted midway between an x-ray tube and an x-ray camera in the planar radiography setting. The grid acted as a transmission grating and cast periodic dark fringes on the camera. The camera had sufficient spatial resolution to resolve the fringes. Refraction and diffraction in the imaged object manifested as position shifts and amplitude attenuation of the fringes, respectively. In order to quantify these changes precisely without imposing a fixed geometric relationship between the camera pixel array and the fringes, a spatial harmonic method in the Fourier domain was developed. The level of the differential phase (refraction) contrast as a function of hardware specifications and device geometry was derived and used to guide the optimal placement of the grid and object. Both *ex vivo* and *in vivo* images of rodent extremities were collected to demonstrate the capability of the method. The exposure time using a 50 W tube was 28 s.
Results: Differential phase contrast images of glass beads acquired at various grid and object positions confirmed theoretical predictions of how phase contrast and extraneous artifacts vary with the device geometry. In anesthetized rats, a single exposure yielded artifact-free images of absorption, differential phase contrast, and diffraction. Differential phase contrast was strongest at bone-soft tissue interfaces, while diffraction was strongest in bone.
Conclusions: The spatial harmonic method allowed us to obtain absorption, differential phase contrast, and diffraction images, all from a single raw image and is feasible in live animals. Because the sensitivity of the method scales with the density of the gratings, custom microfabricated gratings should be superior to off-the-shelf lead grids. [DOI: 10.1118/1.3501311]

Key words: differential phase contrast, spatial harmonics, dark field, scattering, Fourier analysis, CT

I. INTRODUCTION

X-ray phase contrast imaging generally refers to the detection of the refractive bending of x rays in the imaged object. X-ray diffraction, scattering, or dark-field imaging refers to the detection of small-angle coherent scattering of x rays in the object. Initially demonstrated at synchrotron beamlines, phase contrast and diffraction imaging can greatly enhance soft tissue contrast based on their different indices of refraction and reveal pathological changes in the tissue structures not visible in absorption radiography.[1,2] An effective way to obtain full-field differential phase contrast (DPC) and diffraction images in laboratory settings is with grating-based Talbot interferometry.[3–8] This technique utilizes a phase grating in a narrow bandwidth x-ray beam to produce intensity fringes on the camera surface at one-eight of the Talbot distance down beam. X-ray refraction at interfaces in the object results in angular deviation of the transmitted rays, leading to changes in the positions of the fringes. Small-angle scattering in the object disperses a single ray into a small cone after passing through the object and results in reduced amplitude of the fringes. To quantify these changes, a second transmission grating of the same period as the fringes is moved across the camera surface to produce oscillating image intensity, which is recorded in a series of images. While this scanning method offered high spatial resolution, the imaging speed was hampered by the scanning process. Clauser[4] proposed in a patent that by using a detector array that is frequency-matched and phase-locked with the fringe pattern, it should be possible to quantify the changes from a single image. However, such hardware requirement is challenging and limits the flexibility of the device layout.

To overcome the above problems and meet the speed requirement of *in vivo* imaging applications, we demonstrated a variant of the grating-based method: A single-shot technique relying on analysis in the spatial frequency domain after a Fourier transformation.[9–12] It was first described by Takeda *et al.* in 1982 for characterizing shifts of interference fringes, and here we show that it produces diffraction images in addition to refractive phase contrast, all from a single raw image without special requirements on the camera beyond a

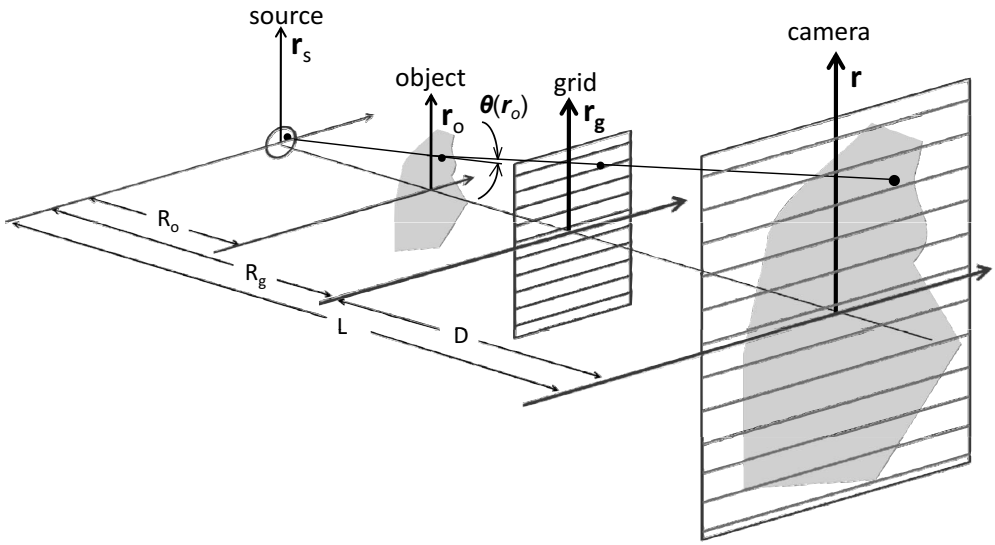

FIG. 1. Layout of the imaging device. From left to right: The x-ray tube, a set of glass beads (object), lead grid, and camera's image plane.

minimum resolution. However, we found that the phase contrast signal contains artifacts from attenuation gradients in the sample and other instrumental factors. We derive design criteria that should be met to remove such artifacts, given a set of hardware specifications including the x-ray tube focal spot size, the camera resolution, and the grating density. We demonstrate the feasibility of this spatial harmonic method in anesthetized rats, which, as far as we can determine, is the first time that such images have been collected *in vivo*.

II. METHODS AND MATERIALS

II.A. System design criteria and sources of artifacts

Here, we show by mathematical derivation the procedure to extract quantitative refraction and diffraction information from a single grating-modulated image. We will explain the two design criteria that must be met to reduce inherent artifacts and the need to correct for the camera point spread function.

The imaging device is illustrated in Fig. 1. The transmission grating in our experiments was a radiography Bucky grid (detailed in Sec. II B) and will be referred to as a grid. The pixel size of the camera should be less than half of the projected period of the grid such that the grid lines can be resolved. We make the following three assumptions in our derivation: (1) We are in the near field condition where $D \ll (\text{grid period})^2/(\text{x-ray wavelength})$ such that wave interference effects are negligible. In this regime, ray-tracing can be used to describe the optics. (2) The object thickness is small such that it can be represented as a two dimensional (2D) transmission function. (3) The solid angle subtended by the image on the camera relative to the source point is small. This is the common small cone angle approximation.

Figure 1 illustrates the device setup with four principle planes. We define two dimensional coordinates in each of these planes, $\boldsymbol{r}$, $\boldsymbol{r}_g$, $\boldsymbol{r}_o$, and $\boldsymbol{r}_s$ for the image, grid, object, and source planes, respectively. The various distances of R_o, R_g, D, and L are also defined in Fig. 1. We further define the transmission function of the object as $M(\boldsymbol{r}_o)$, the brightness distribution of the x-ray source as $B(\boldsymbol{r}_s)$, the size of the source focal spot as S, the grid period as P_0, and the image as $I(\boldsymbol{r})$.

X-ray refraction and small-angle diffraction in the sample are represented in the ray-tracing picture as follows: A single x ray emanating from point $\boldsymbol{r}_s$ on the source hits point $\boldsymbol{r}_o$ on the object plane and undergoes refractive bending such that the emerging ray deviates from the straight line by the angle $\boldsymbol{\theta}(\boldsymbol{r}_o)$; due to small-angle scattering, the emerging x ray from point $\boldsymbol{r}_o$ becomes a dispersed cone centered around the $\boldsymbol{\theta}(\boldsymbol{r}_o)$ line, with a normalized angular distribution $\sigma(\boldsymbol{r}_o, \boldsymbol{\theta}' - \boldsymbol{\theta}(\boldsymbol{r}_o))$.

Figure 2 illustrates the 2D Fourier transformation of the image $I(\boldsymbol{r})$ into the spatial frequency spectrum (SFS) $I'(\boldsymbol{k})$. A detailed derivation in the Appendix shows that the SFS is the sum of a series of harmonic spectra, each centered at an integer multiple of the projected grid frequency on the image plane $n\boldsymbol{g}$, where $\boldsymbol{g} = (2\pi/P_0)(R_g/L)$.

The spatial harmonic method relies on being able to obtain images from individual harmonic spectra. This is pos-

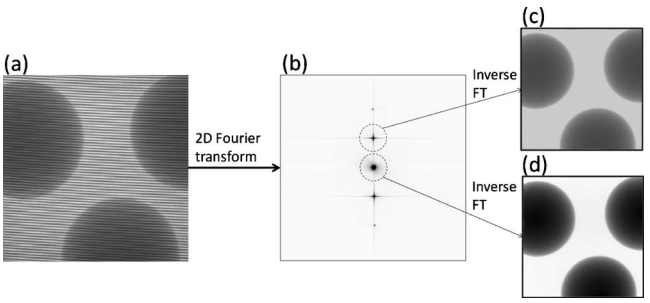

FIG. 2. Retrieval of harmonic images and differential phase contrast in the spatial frequency domain. (a) Raw image. The Moiré pattern in this image is due to subsampling to reduce the size of the figure for publication. (b) 2D spatial spectrum of raw image, (c) first-order harmonic image, and (d) zeroth-order (absorption) image.

sible if the individual harmonic spectra are cleanly separated in the spatial frequency domain, and the first-order harmonic spectrum has sufficient amplitude. In the Appendix, we show that these conditions lead to two design requirements,

$$E_1 = \frac{S}{P_0}\frac{D}{L} \ll 1, \tag{1}$$

$$E_2 = \frac{S}{P_0}\frac{L-R_o}{R_o}\frac{R_g}{L} > 1. \tag{2}$$

Then, the first-order harmonic image is obtained from the inverse Fourier transformation of the segment of the SFS that is centered at the peak position $\boldsymbol{g}$,

$$H_1(\vec{r}) = \Im^{-1}(H'_1),$$

$$H'_1(\vec{q}) \approx I'(\vec{q}+\vec{g}), |\vec{q}| \le |\vec{g}|/2. \tag{3}$$

Generally, a harmonic image is complex valued, and we show in the Appendix that it contains information about the refraction angle $\boldsymbol{\theta}(\boldsymbol{r_o})$ and small-angle scattering $\sigma(\boldsymbol{r_o}, \boldsymbol{\theta'} - \boldsymbol{\theta}(\boldsymbol{r_o}))$,

$$H_n(\vec{r}) \approx \left\{ M\left(\frac{R_o}{L}\vec{r}\right)\exp\left[i\vec{C}_n \cdot \vec{\theta}\left(\frac{R_o}{L}\vec{r}\right)\right] + i\vec{\delta}_n \cdot \left[(\nabla M)\left(\frac{R_o}{L}\vec{r}\right) + (\nabla \sigma_n{}') \times \left(\frac{R_o}{L}\vec{r}\right)\right]\right\} \sigma_n{}'\left(\frac{R_o}{L}\vec{r}\right), \tag{4}$$

where

$$|\vec{C}_n| = n\frac{R_o}{L}D\frac{2\pi}{P_0},$$

$$|\vec{\delta}_n| = n\frac{S^2(L-R_o)D}{L^2}\frac{\pi}{P_0}, \tag{5}$$

and $\sigma_n{}'$ is the Fourier transform of the small-angle scattering distribution σ,

$$\sigma_n{}'\left(\frac{R_o}{L}\vec{r}\right) = \int\int \sigma\left(\frac{R_o}{L}\vec{r}, \vec{\theta}' - \vec{\theta}\left(\frac{R_o}{L}\vec{r}\right)\right)\exp(i\vec{C}_n \cdot \vec{\theta}')d^2\theta'. \tag{6}$$

The parameter C_n is the conversion factor between the x-ray refraction angle in the sample and the phase shift in the harmonic image. The differential phase contrast signal, as defined in prior literature,[6,13,14] is indeed this phase shift. C_n represents the phase contrast sensitivity of the imaging device and is called the refraction angle to phase-shift (RAPS) conversion factor in the following text. Its expression in Eq. (5) shows that larger distances between the grid and the camera lead to higher refraction sensitivity. However, D cannot be too large as to violate the criterion of Eq. (1).

The parameter δ_n controls the amplitude of an extraneous contribution to the phase contrast signal, which comes from the spatial gradient of attenuation and diffraction in the sample. This is an inherent artifact in single-image based Fourier space fringe analysis. It is minimized when the design criterion of $E_1 \ll 1$ is met.

The factor $\sigma_n{}'$ represents attenuation of the amplitude of the harmonic image by small-angle diffraction. Because of the normalization condition of the scattering distribution σ, $\sigma_0{}' = 1$. It means that the zeroth-order image is not affected by diffraction. By taking the ratio between the first- and the zeroth-order images, we obtain a pure diffraction image

$$\frac{|H_1(\vec{r})|}{|H_0(\vec{r})|} \approx \sigma_1{}'\left(\frac{R_o}{L}\vec{r}\right). \tag{7}$$

By modeling the object as a stack of infinitesimal layers, it can be shown that the logarithm of this ratio is proportional to the object thickness.[9] For this reason, the diffraction image is usually displayed in log scale.

The design criteria of Eqs. (1) and (2) impose conditions on the focal spot size of the x-ray tube S, the grid density, and the geometry of the device layout. Criterion 1 is met by selecting x-ray tubes with focal spot sizes less than the grid period; criterion 2 can be met by making R_o sufficiently small by placing the object sufficiently close to the source. An alternative way to meet the first criterion is to place a second transmission grating right in front of the source, which has been employed in the previous Talbot interferometry methods.[6,15] The trade-off of this approach is an increased device complexity and a reduction in the amplitude of the first-order harmonics.

We will show experimentally the artifacts in the DPC images when the criterion of Eq. (2) is not met. We also varied the RAPS conversion factor by varying the grid-to-camera distance D and measured the corresponding changes in the DPC values. Particularly, we found that the DPC did not diminish when D approached zero. This turned out to be due to the point spread function (PSF) of the camera.[16–18] The PSF of the camera is mostly determined by light scattering within the phosphor screen used to convert x rays to visible light.[19] The SFS of the measured image, $J'(\boldsymbol{k})$, is a combination of the true SFS, $I\prime(\boldsymbol{k})$, and the Fourier transform of the camera PSF, $C\prime(\boldsymbol{k})$,

$$J'(\vec{k}) = I'(\vec{k})C'(\vec{k}). \tag{8}$$

Within the fraction of the SFS that surrounds a nonzero harmonic peak, the shape of $C'(\boldsymbol{k})$ is asymmetric and therefore introduces an extraneous phase to the harmonic image. In order to correct for this effect, we measured the PSF of the camera using a narrow slit and calculated the true SFS of the image,

$$I'(\vec{k}) = \frac{J'(\vec{k})}{C'(\vec{k})}. \tag{9}$$

This division in the spatial spectral domain is equivalent to a deconvolution in the image domain. Deconvolution is a common method for correcting the PSF of a camera detector.[17] Here, it is valid for spatial frequencies where the Fourier transform of the PSF does not diminish. In our device, the full width at half maximum of the camera's PSF is about

TABLE I. Design criteria and phase multiplier for the grid and object placements that were tested.

APP	R_o (cm)	Criterion 1 $E_1 \ll 1$	Criterion 2 $E_2 > 1$	RAPS $DR_o g_0/L$
47.5	50	0.1861	0.2097	11 750
47.5	12	0.1861	1.531	2820
50.5	12	0.1978	1.445	2983
10.5	12	0.041 13	2.600	620.3
5.5	12	0.021 55	2.745	324.9

120 μm. The period of the grid projected onto the camera is 256 μm when $D=50.5$ cm. Therefore, $C'(\boldsymbol{k})$ had sufficient amplitude at the first harmonic spectrum for the PSF correction.

II.B. Device setup

The imaging device consisted of a 50 W tungsten-target x-ray tube of 50 μm focal spot operating at 50 kVp/1 mA (SB-80-1k, Source Ray Inc.), an x-ray camera consisting of a 16 bit water-cooled CCD array of matrix size of 2045 $\times$2048 and pixel size of 30 μm, coupled to a $Gd_2O_2S:Tb$ phosphor screen via a 1:1 fiber-optic taper (PI-SCX-4096, Princeton Instruments), and a radiography Bucky grid acting as a transmission grating. The exposure time was 28 s. The radiation dose for this length of exposure was 0.61 mSv, which is at the level of a lateral chest diagnostic x ray.[20] The x-ray source has a beryllium window, and the grid effectively adds 1.7 mm of aluminum filtration. No other filters were used. The resulting half-value layer of the cone beam was 1.3 mm of Al. Based on Refs. 21 and 22, the spectrum of the tube operating at 50 kVp peaks at approximately 27 keV and has a full width half height of approximately 20 keV.

The Bucky grid contained layers of alternating strips of lead and aluminum. Typically, these grids are specified by the ratio of the height of the strips to the width of the passing slits. The ratios run from 5:1 to 12:1. Also, the grids are focused by tilting the lead strips so that their projections converge at a set distance from the grid. The x-ray source acts as a point source, so the strips are angled such that they face the source when it is placed at a set distance. We used a 200 lines/in. grid (78.74 lines/cm) with a 6:1 ratio, with a nominal focal distance of 51 cm (20 in.).

The total distance between the source and the camera (L) was 100 cm. We tested five sets of distances between the camera and the grid D, and between the imaged object and the focal spot R_0 (see Table I). The ratios E_1 and E_2 specified in the system design criteria of Eqs. (1) and (2) and the RAPS factor representing phase contrast sensitivity were also tabulated for the various geometries. In the design tests the objects being imaged were a set of glass beads 5 mm in diameter. The first setting violated criterion 2, which is that the harmonic spectra should not overlap. The other settings satisfied both criteria. In the last three settings, we tested a range of distance D. Since the RAPS factor scales directly with D, the DPC signal level at $D=5.5$ cm should be about one-tenth of the one at $D=50.5$ cm. These three sets were processed with and without camera's PSF correction to study its effect.

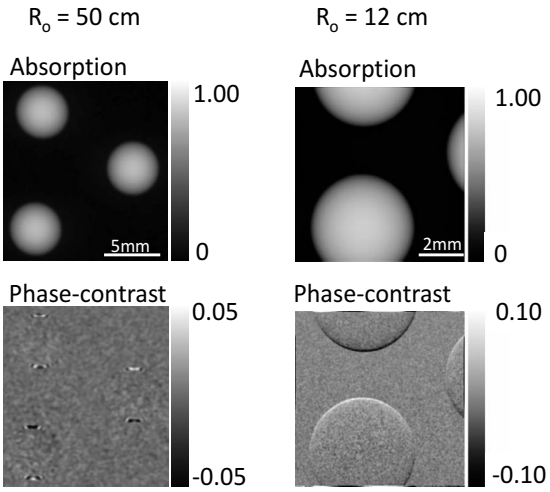

FIG. 3. Glass beads at different distances from the x-ray source. Top row: Absorption images for $R_o=50$ and 12 cm. Bottom row: Differential phase contrast images for $R_o=50$ and 12 cm.

II.C. *Ex vivo* and *in vivo* animal imaging experiments

Finally, we took images of a euthanized mouse and a live rat under Institutional Animal Care and Use Committee approved protocol. For the mouse, we took sagittal images of its snout and the surrounding region. For these images, $D=50.5$ cm and $R_o=16.5$ cm. An adult male rat was sedated first with isoflurane and injected via the tail vein with 60 mg/kg ketamine and 7.5 mg/kg xylazine to keep it under anesthesia for a few minutes. We obtained coronal images of both front and back paws. For the rat images, $D=51.3$ cm and $R_o=13.3$ cm. The corresponding phase contrast sensitivity to x-ray refraction was 3.4×10^3 rad/rad.

III. RESULTS

Images of the glass beads from the first two settings in Table I of $R_o=50$ cm and $R_o=12$ cm were compared in Fig. 3. We expect to see DPC signal at the top and bottom edges of the glass beads where x rays were slightly bent by refraction in a direction that is not parallel to the grid lines. The results showed similar absorption images at both settings, but a marked difference in the DPC images. When the beads were at 50 cm from the x-ray source, criterion 2 was not met. The top and bottom edges of the beads were visible at a few spots, as what appeared to be ringing artifacts. When the beads were placed at 12 cm from the source, the edges were clearly visible without artifacts. These images show that the second criterion of no overlap between harmonic spectra needs to be met to obtain artifact-free DPC images.

In the next three settings, where we looked at the dependence of the DPC signal on the grid-to-camera distance D, it was evident that we needed to correct for the camera's point spread function. Images from these three settings with and without the PSF correction are shown in Fig. 4. As one can

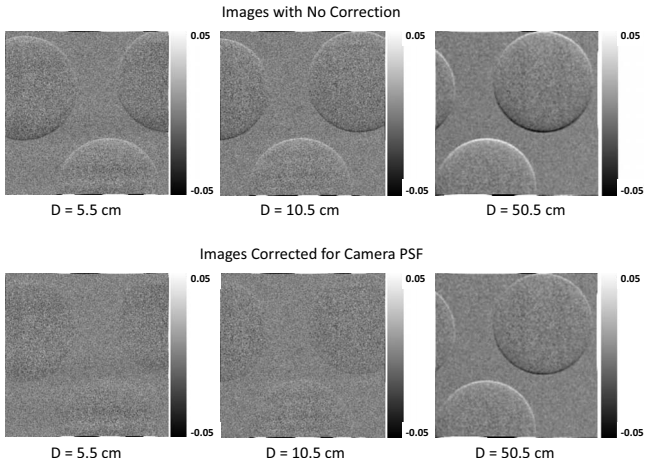

FIG. 4. Differential phase contrast images of glass beads acquired at the last three system geometry settings listed in Table I. Top row: Images without camera correction with the grid set at three different distances from the camera. Bottom row: Images at the same distances but with correction for the camera's point spread function.

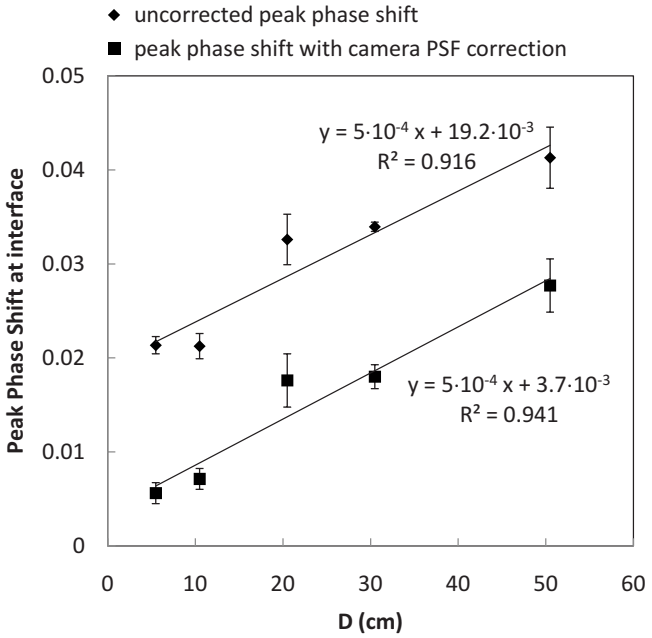

FIG. 5. The differential phase contrast signal at the top and bottom edges of the glass beads as a function of the grid-to-camera distance D, with and without camera's PSF correction. The extraneous phase at low D values was an effect of the camera's point spread function. The error bars indicate 1 standard deviation.

see in the DPC images, there was a substantial residual signal at the lowest D setting without PSF correction, as opposed to what we expected from the theoretical analysis. This was removed with the camera correction. Figure 5 quantifies the amplitudes of the DPC signal at the top and bottom edges of the beads with and without camera correction. Overall, we see that placing the object at $R_o = 12$ and the grid at $D = 50$ cm provides good DPC image quality with adequate resolution.

We tested the optimal setting in a mouse *ex vivo* and successfully imaged a rat *in vivo*. The images of the mouse's snout region are shown in Fig. 6. The images of the front and back paws of a live rat are shown in Fig. 7. In these images the differential phase contrast is most visible at interfaces between the bone and the soft tissue. In the phase maps, the minimum detectable phase shift, as defined to be twice the noise fluctuation, is 0.0072 rad. By the RAPS conversion factor, the minimum detectable x-ray refraction in the sample was 2.1 μrad. The diffraction effect is also most prominent in bone, as seen in prior studies.[23–26] A plot of absorption vs diffraction for the bone areas of the rat foot is shown in Fig. 8. The interpretation of diffraction signal in bone obtained with this technique has been investigated in detail in a previous *in vitro* study.[23]

IV. CONCLUSION

Previous works have shown that in a grating-modulated projection image, x-ray refraction can be extracted through the phase shift of harmonic images obtained in the spatial frequency domain.[9–12,27] Here, we show that the amplitude of the harmonic images relates to the small-angle scattering distribution by a Fourier transform. We also show that the phase contrast obtained by this method contains extraneous terms besides refraction, both from the sample itself as well as the imaging device. With judicious layout of the imaging device and correction for the camera's point spread function, we can obtain artifact-free differential phase contrast and diffraction images. This method has allowed us to do *in vivo* animal imaging in a reasonable time with radiation exposure comparable to current diagnostic x-ray imaging.

As can be seen from the definition of the design parameters E_1 and E_2, the energy spectrum of the x-ray tube does not affect the system design directly. Since our device operated in the near field condition, the grating fringe visibility was also not affected by the energy spectrum. However, because in most materials the refractive index and the scattering cross section vary with the x-ray energy, this ultimately affects the level of refraction and diffraction contrast that are obtained with this technique.

The fundamental limitation of the spatial harmonic method is that in order to resolve the grating lines on the camera, the size of the camera pixel needs to be equal to or less than one-third of the projected grating period. This sets the upper limit of the grating density. The analysis of Eq. (3) shows that the lower the grating density, the lower the sensitivity of the differential phase contrast. One solution to this problem is to convert a high density grating pattern into a low density Moiré pattern by using a second transmission grating on the camera surface.[28] The Moiré pattern can then be directly resolved by the camera. However, the contrast of the Moiré pattern will not be as high as the underlying grating fringes. A more efficient solution may lie in high resolution x-ray cameras. Single-crystal scintillators have demonstrated submicron resolution,[27,29] and recently micron resolution x-ray cameras are becoming commercially available (e.g., Xsight from Rigaku) for up to 10 keV photon

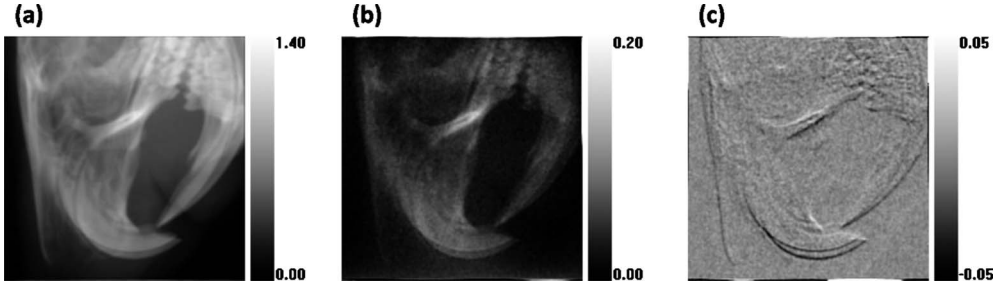

FIG. 6. Mouse snout taken *ex vivo* with correction for camera PSF; (a) absorption image, (b) diffraction image, and (c) DPC image.

energy. If these cameras reach sufficient quantum efficiency at higher energies, they should provide the ultimate solution to overcome the sensitivity limits.

ACKNOWLEDGMENTS

The authors are grateful to Joni Taylor and Kathy Lucas for the care and handling of the animals.

APPENDIX: DERIVATION OF PHASE-CONTRAST AND DARK-FIELD IMAGES FROM SPATIAL HARMONICS FOR OPTICAL NEAR FIELD REGIME

Referring to Fig. 1, the image intensity, $I(\boldsymbol{r})$, can be expressed in terms of the transmission functions of the object, $M(\boldsymbol{r_o})$, the grid, $T(\boldsymbol{r_g})$, and the brightness distribution of the x-ray source, $B(\boldsymbol{r_s})$,

$$I(\vec{r}) = \int\int M(\vec{r}_o)T(\vec{r}_g)B(\vec{r}_s)d^2r_s. \tag{A1}$$

The grid transmission function can be defined as a Fourier series,

$$T(\vec{r}_g) = \sum_{n=-\infty}^{\infty} c_n \exp(in\vec{g}_0 \cdot \vec{r}_g), \tag{A2}$$

where $g_0 = 2\pi/P_0$ and P_0 is the grid period. We can determine the trajectory of the x-ray from the device geometry in Fig. 1,

$$\vec{r}_o = \vec{r}_s + (\vec{r} - \vec{r}_s)\frac{R_o}{L} + \vec{\delta}_o, \tag{A3}$$

$$\vec{r}_g = \vec{r}_s + (\vec{r} - \vec{r}_s)\frac{R_g}{L} + \vec{\delta}_g. \tag{A4}$$

The vectors $\boldsymbol{\delta_o}$ and $\boldsymbol{\delta_g}$ are small displacements from the straight line trajectory due to the refractive bending angle $\boldsymbol{\theta}(\boldsymbol{r_o})$.

We note that

$$\vec{\delta}_g = \frac{R_o}{L} D\vec{\theta}(\vec{r}_o), \tag{A5}$$

which represents a change in the position of the grid lines on the image plane due to refraction. In prior literature, this shift has been defined as the differential phase contrast. Our aim is to retrieve this quantity.

For further derivation, we assume that the object transmission function does not change over the small distance $\boldsymbol{\delta_o}$. We define the following projection functions onto the image plane:

$$M_p(\vec{r}) = M\left(\frac{R_o}{L}\vec{r}\right), \tag{A6}$$

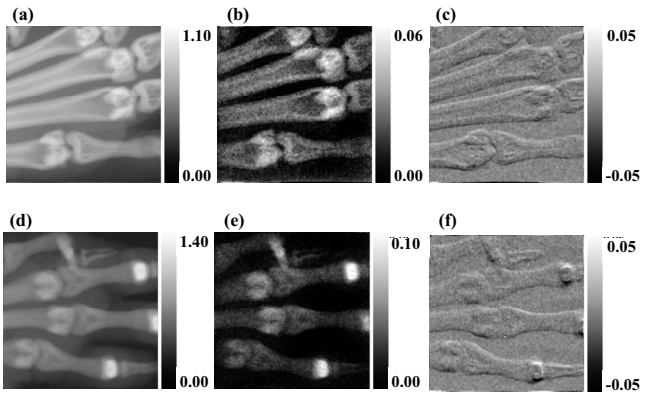

FIG. 7. Images of rat paws taken *in vivo*, with camera's PSF correction. (a) Back paw, absorption image; (b) back paw, diffraction image; (c) back paw, DPC image; (d) front paw, absorption image; (e) front paw, diffraction image; and (f) front paw, DPC image.

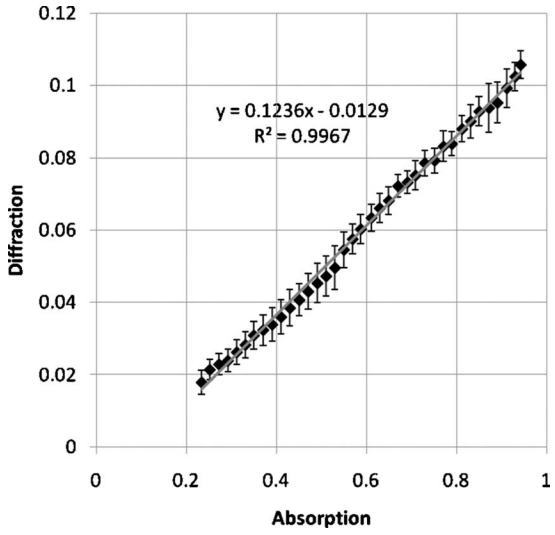

FIG. 8. X-ray absorption vs. diffraction in the bone sections of the rat foot images. Error bars show one standard deviation.

$$\vec{\theta}_p(\vec{r}) = \vec{\theta}\left(\frac{R_o}{L}\vec{r}\right), \tag{A7}$$

$$\vec{g} = \vec{g}_0\frac{R_g}{L}, \tag{A8}$$

$$B_p(\vec{r}) = B\left(-\vec{r}\frac{R_o}{L-R_o}\right). \tag{A9}$$

We further define for any integer n,

$$M_n(\vec{r}) = M_p(\vec{r})\exp\left[in\frac{R_o}{L}D\vec{g}_0\cdot\vec{\theta}_p(\vec{r})\right]. \tag{A10}$$

Then, the 2D Fourier transform of the image $I(\boldsymbol{r})$ is

$$I'(\vec{k}) = \sum_n c_n M'_n(\vec{k}-n\vec{g})B'_p[(\vec{k}-n\vec{g})+\beta n\vec{g}], \tag{A11}$$

where M'_n and B'_p are the 2D Fourier transforms of M_n and B_p, and

$$\beta = \frac{R_o D}{R_g(L-R_o)}. \tag{A12}$$

Equation (A11) shows that the SFS of the raw image $I'(\boldsymbol{k})$ is the sum of a series of harmonic spectra, each centered at $n\boldsymbol{g}$. This is illustrated in Fig. 2. We define the nth order harmonic spectrum as follows:

$$H'_n(\vec{k}-n\vec{g}) = M'_n(\vec{k}-n\vec{g})B'_p[(\vec{k}-n\vec{g})+\beta n\vec{g}]. \tag{A13}$$

In order to reconstruct harmonic images from the individual harmonic spectra, they need to be cleanly separated in the spatial frequency domain. This means that the bandwidth of each spectrum in the direction of $\boldsymbol{g}$, or perpendicular to the grid lines, should be less than the primary grid frequency $|\boldsymbol{g}|$ (Fig. 2),

$$H'_n(\vec{q}) \approx 0 \quad for\ |\vec{q}| > |\vec{g}|/2. \tag{A14}$$

Second, the first-order harmonics ($n=\pm 1$) should have substantial amplitudes. These two criteria are met if

$$B'_p(\beta\vec{g}) \approx B'_p(0),$$

$$B'_p(\vec{q}+\beta\vec{g}) \approx 0 \quad for\ |\vec{q}| > |\vec{g}|/2. \tag{A15}$$

These translate to requirements on the hardware specifications and device layout, which are expressed in Eqs. (1) and (2) of the main text. When both are met, the nth harmonic spectrum can be obtained from the segment of the SFS, which is centered at the peak position $n\boldsymbol{g}$,

$$H'_n(\vec{q}) \approx I'(\vec{q}+n\vec{g}), \quad |\vec{q}| \le |\vec{g}|/2. \tag{A16}$$

Then, a harmonic image can be formed by taking the inverse Fourier transform of H_n'. From Eq. (A13),

$$H_n(\vec{r}) = \Im^{-1}(H'_n) = M_n(\vec{r}) \otimes [B_p(\vec{r})\exp(in\beta\vec{g}\cdot\vec{r})]. \tag{A17}$$

Assuming that the source brightness distribution follows a Gaussian,

$$B(\vec{r}_S) = B_0 e^{-(\vec{r}_s/S)^2}, \tag{A18}$$

then

$$H_n(\vec{r}) \approx M\left(\frac{R_o}{L}\vec{r}\right)\exp\left[i\vec{C}_n\cdot\vec{\theta}\left(\frac{R_o}{L}\vec{r}\right)\right] + i\vec{\delta}_n\cdot(\nabla M)\left(\frac{R_o}{L}\vec{r}\right), \tag{A19}$$

where

$$\vec{C}_n = n\frac{R_o}{L}D\vec{g}_0,$$

$$\vec{\delta}_n = n\frac{S^2(L-R_o)D}{2L^2}\vec{g}_0. \tag{A20}$$

Now we consider the effect of small-angle scattering. In the ray-tracing picture of Fig. 1, the emerging x ray from point $\boldsymbol{r_o}$ in the object becomes a dispersed cone centered around the $\boldsymbol{\theta}(\boldsymbol{r_o})$ line, with a normalized angular distribution $\sigma(\boldsymbol{r_o}, \boldsymbol{\theta'}-\boldsymbol{\theta}(\boldsymbol{r_o}))$,

$$\int\int \sigma(\vec{r}_o, \vec{\theta}' - \vec{\theta}(\vec{r}_o))d^2\vec{\theta}' = 1. \tag{A21}$$

Equation (A1) is modified to

$$I(\vec{r}) = \int\int d^2\vec{r}_s \int\int d^2\vec{\theta}' M(\vec{r}_o + (L-R_o)\vec{\theta}')T \times\left(\vec{r}_g + \frac{R_o}{L}D\vec{\theta}'\right)\sigma(\vec{r}_o, \vec{\theta}' - \vec{\theta}(\vec{r}_o))B(\vec{r}_s). \tag{A22}$$

Repeating the same derivation from Eq. (A1) to Eq. (A11) gives a modified version of Eq. (A10),

$$M_n(\vec{r}) = M_p(\vec{r})\sigma'_n\left(\frac{R_o}{L}\vec{r}\right)\exp\left[in\frac{R_o}{L}D\vec{g}_0\cdot\vec{\theta}_p(\vec{r})\right], \tag{A23}$$

where

$$\sigma'_n\left(\frac{R_o}{L}\vec{r}\right) = \int\int \sigma\left(\frac{R_o}{L}\vec{r}, \vec{\theta}' - \vec{\theta}_p(\vec{r})\right) \times\exp\left(in\frac{R_o}{L}D\vec{g}_0\cdot\vec{\theta}'\right)d^2\theta'. \tag{A24}$$

Substituting Eq. (A23) into Eq. (A17) yields Eq. (4) in the main text, which is the complete expression of the nth order harmonic image.

[a]Electronic mail: bennette@nhlbi.nih.gov
[b]Author to whom correspondence should be addressed. Electronic mail: wenh@nhlbi.nih.gov

[1]M. N. Wernick, O. Wirjadi, D. Chapman, Z. Zhong, N. P. Galatsanos, Y. Y. Yang, J. G. Brankov, O. Oltulu, M. A. Anastasio, and C. Muehleman, "Multiple-image radiography," Phys. Med. Biol. **48**, 3875–3895 (2003).
[2]T. Kao, D. Connor, F. A. Dilmanian, L. Faulconer, T. Liu, C. Parham, E. D. Pisano, and Z. Zhong, "Characterization of diffraction-enhanced imaging contrast in breast cancer," Phys. Med. Biol. **54**, 3247–3256 (2009).
[3]S. Yokozeki and T. Suzuki, "Shearing interferometer using grating as beam splitter," Appl. Opt. **10**, 1575–1580 (1971).
[4]J. F. Clauser, US Patent No. 5,812,629 (22 September 1998).
[5]A. Momose, S. Kawamoto, I. Koyama, Y. Hamaishi, K. Takai, and Y. Suzuki, "Demonstration of x-ray Talbot interferometry," Jpn. J. Appl. Phys., Part 2 **42**, L866–L868 (2003).

[6]T. Weitkamp, A. Diaz, C. David, F. Pfeiffer, M. Stampanoni, P. Cloetens, and E. Ziegler, "X-ray phase imaging with a grating interferometer," Opt. Express **13**, 6296–6304 (2005).
[7]F. Pfeiffer, C. Kottler, O. Bunk, and C. David, "Hard x-ray phase tomography with low-brilliance sources," Phys. Rev. Lett. **98**, 108105 (2007).
[8]Y. Takeda, W. Yashiro, Y. Suzuki, S. Aoki, T. Hattori, and A. Momose, "X-ray phase imaging with single phase grating," Jpn. J. Appl. Phys., Part 2 **46**, L89–L91 (2007).
[9]H. Wen, E. Bennett, M. M. Hegedus, and S. C. Carroll, "Spatial harmonic imaging of x-ray scattering-initial results," IEEE Trans. Med. Imaging **27**, 997–1002 (2008).
[10]H. Wen, E. E. Bennett, M. M. Hegedus, and S. Rapacchi, "Fourier x-ray scattering radiography yields bone structural information," Radiology **251**, 910–918 (2009).
[11]M. Takeda, H. Ina, and S. Kobayashi, "Fourier-transform method of fringe-pattern analysis for computer-based topography and interferometry," J. Opt. Soc. Am. **72**, 156–160 (1982).
[12]A. Momose, W. Yashiro, H. Kuwabara, and K. Kawabata, "Grating-based x-ray phase imaging using multiline x-ray source," Jpn. J. Appl. Phys. **48**, 076512 (2009).
[13]B. C. Platt and R. Shack, "History and principles of Shack-Hartmann wavefront sensing," J. Refract. Surg. **17**, S573–S577 (2001).
[14]S. C. Mayo and B. Sexton, "Refractive microlens array for wave-front analysis in the medium to hard x-ray range," Opt. Lett. **29**, 866–868 (2004).
[15]D. W. Keith, C. R. Ekstrom, Q. A. Turchette, and D. E. Pritchard, "An interferometer for atoms," Phys. Rev. Lett. **66**, 2693–2696 (1991).
[16]M. Pilz, S. Honold, and A. Kienle, "Determination of the optical properties of turbid media by measurements of the spatially resolved reflectance considering the point-spread function of the camera system," J. Biomed. Opt. **13**, 054047 (2008).
[17]M. Zhang, Q. Chen, X. F. Li, J. O'Donoghue, S. Ruan, P. Zanzonico, C. C. Ling, and J. L. Humm, "Image deconvolution in digital autoradiography: A preliminary study," Med. Phys. **35**, 522–530 (2008).
[18]A. R. Faruqi, Design principles and applications of a cooled CCD camera for electron microscopy (1998).
[19]R. M. Nishikawa, M. J. Yaffe, and R. B. Holmes, "Effect of finite phosphor thickness on detective quantum efficiency," Med. Phys. **16**, 773–780 (1989).
[20]C. J. Martin, "Radiation dosimetry for diagnostic medical exposures," Radiat. Prot. Dosim. **128**, 389–412 (2008).
[21]M. Bhat, J. Pattison, G. Bibbo, and M. Caon, "Diagnostic x-ray spectra: A comparison of spectra generated by different computational methods with a measured spectrum," Med. Phys. **25**, 114–120 (1998).
[22]M. M. Blough, R. G. Waggener, W. H. Payne, and J. A. Terry, "Calculated mammographic spectra confirmed with attenuation curves for molybdenum, rhodium, and tungsten targets," Med. Phys. **25**, 1605–1612 (1998).
[23]Y. Liu, H. Wen, R. C. Gorman, J. J. Pilla, J. H. Gorman, G. Buckberg, S. D. Teague, and G. S. Kassab, "Reconstruction of myocardial tissue motion and strain fields from displacement-encoded MR imaging," Am. J. Physiol. Heart Circ. Physiol. **297**, H1151–H1162 (2009).
[24]T. Weitkamp, C. David, O. Bunk, J. Bruder, P. Cloetens, and F. Pfeiffer, "X-ray phase radiography and tomography of soft tissue using grating interferometry," Eur. J. Radiol. **68**, S13–S17 (2008).
[25]M. Bech, T. H. Jensen, R. Feidenhans'l, O. Bunk, C. David, and F. Pfeiffer, "Soft-tissue phase-contrast tomography with an x-ray tube source," Phys. Med. Biol. **54**, 2747–2753 (2009).
[26]T. Donath, F. Pfeiffer, O. Bunk, C. Grunzweig, E. Hempel, S. Popescu, P. Vock, and C. David, "Toward clinical x-ray phase-contrast CT demonstration of enhanced soft-tissue contrast in human specimen," Invest. Radiol. **45**, 445–452 (2010).
[27]A. Momose, "High-speed x-ray phase imaging and x-ray phase tomography with Talbot interferometer and white synchrotron radiation," Opt. Express **17**, 12540–12545 (2009).
[28]C. David, B. Nohammer, H. H. Solak, and E. Ziegler, "Differential x-ray phase contrast imaging using a shearing interferometer," Appl. Phys. Lett. **81**, 3287–3289 (2002).
[29]A. Koch, C. Raven, P. Spanne, and A. Snigirev, "X-ray imaging with submicrometer resolution employing transparent luminescent screens," J. Opt. Soc. Am. A Opt. Image Sci. Vis **15**, 1940–1951 (1998).